Key Points:
- Simulated the excitation and propagation of EMIC waves in 2D dipole fields
- Proposed a novel method for WNA diagnosis in simulations
- The propagation effect of waves turning oblique leads to the linear polarization of EMIC waves at high latitudes

Correspondence to:
Q. Lu and X. Gao,
qmlu@ustc.edu.cn;
gaoxl@mail.ustc.edu.cn

Author Contributions:
Conceptualization: Ning Kang, Xinliang Gao
Formal analysis: Ning Kang
Investigation: Ning Kang, Xinliang Gao
Methodology: Ning Kang
Project Administration: Quanming Lu, Xinliang Gao
Software: Xueyi Wang
Supervision: Quanming Lu, Xinliang Gao, Shui Wang
Writing – original draft: Ning Kang
Writing – review & editing: Ning Kang, Quanming Lu, Xinliang Gao, Huayue Chen

Propagation of Electromagnetic Ion Cyclotron Waves in a Dipole Magnetic Field: A 2-D Hybrid Simulation

Ning Kang[1,2] ⓘ, Quanming Lu[2,3] ⓘ, Xinliang Gao[2,3] ⓘ, Xueyi Wang[4] ⓘ, Huayue Chen[2,3] ⓘ, and Shui Wang[2,3]

[1]Department of Atmospheric and Oceanic Sciences, University of California, Los Angeles, CA, USA, [2]CAS Key Lab of Geospace Environment, School of Earth and Space Sciences, University of Science and Technology of China, Hefei, China, [3]CAS Center for Excellence in Comparative Planetology, Hefei, China, [4]Physics Department, Auburn University, Auburn, AL, USA

Abstracts Electromagnetic ion cyclotron (EMIC) waves are one commonly observed plasma waves in the Earth's inner magnetosphere and play a crucial role in particle dynamics in the radiation belt and ring current. EMIC waves are excited by a proton temperature anisotropy and generally have a left-handed polarization, however satellite observations have usually reported the existence of linearly polarized EMIC waves in the inner magnetosphere. In this paper, we employ a two-dimensional (2D) hybrid code in a dipole field (gcPIC-hybrid) to simulate the propagation of EMIC waves from the equatorial source region. We track one single EMIC wave packet and analyze how its properties evolve along its trajectory. In diagnosing the wave normal angle (WNA) of the packet, we propose a novel method called Wave Front Shape Identification (WFSI). The ellipticity can also been calculated after we know the WNA. By comparing the ellipticity calculated from the linear theory and the ellipticity diagnosed from the simulation, we conclude that in a proton-electron plasma, EMIC waves would turn from a left-handed polarization to a linear polarization solely due to the propagation effect when the waves propagate toward higher latitudes and become oblique. We also find that the peak frequency of the wave packet (the wave mode with the maximum amplitude) decreases when propagating toward higher latitudes, which is due to different growth and damping behavior of different modes.

1. Introduction

Electromagnetic ion cyclotron (EMIC) waves are a commonly observed plasma waves in the Earth's inner magnetosphere (Anderson et al., 1990; Thorne, 2010; Young et al., 1981), which are excited by anisotropic energetic protons through the cyclotron instability (Davidson & Ogden, 1975; Gary & Lee, 1994; Yue et al., 2019). These anisotropic protons are originated either from a substorm injection or solar wind compression (Chen et al., 2020). Numerous observational and theoretical works have associated EMIC waves with the scattering and precipitation of relativistic electrons, and implied that EMIC waves could be a main contributor of relativistic electron loss in the radiation belt (e.g., Chen et al., 2016; Denton et al., 2019; Li et al., 2007; Ni et al., 2015; Omura & Zhao, 2012; Thorne & Kennel, 1971; Zhang et al., 2016). Moreover, EMIC waves can also lead to the heating of thermal ions, especially heavy ion species, via bi-ion resonance or resonance with harmonic of gyrofrequency (Fuselier & Anderson, 1996; Ma et al., 2019; Thorne & Horne, 1994).

EMIC waves excited by the ion temperature anisotropy in a homogeneous plasma usually propagate along the background magnetic field, and have a left-handed polarization. However, satellite observations have indicated that the EMIC waves in the radiation belt usually have a linear polarization (Anderson et al., 1992; Fraser, 1985; Young et al., 1981). Recently, statistical works conducted by Chen et al., 2019, Allen et al., 2015 and Min et al., 2012 have shown that EMIC waves tend to have a negative ellipticity of about −0.3 near the equator, but have a near zero ellipticity at higher latitudes. This implies that EMIC waves turn from a left-handed polarization to a linear polarization as they propagate to high latitudes. Along with the increased ellipticity, the wave normal angle (WNA) increases, which is as small as several degrees near the equator but up to 60° at high latitudes.

There have been several proposals to explain the linear polarization of EMIC waves in the radiation belt. It could be a propagation effect, as a direct result of waves turning oblique (Denton et al., 1992) or crossover effect when there are heavier ions (André, 1985; Smith and Brice, 1964). Certain plasma condition in the source region, for example, loss cone distribution of hot ions (Denton et al., 1992) or high beta multi-ion plasma (Remya et al., 2017), can excite oblique EMIC waves with linear or even right-handed polarization. Also, when the

observed EMIC waves are a superposition of two or more left-handed waves, it could also "look like" a linearly or even right-handed polarized waves (Denton et al., 1996). However, which one works in a real radiation belt is still unknown.

Kinetic simulation provides a powerful tool to examine these theories. Two-dimensional hybrid simulations of EMIC waves excited by the ion temperature anisotropy have been fulfilled in a dipole magnetic field (Denton, 2018; Denton et al., 2014; Hu & Denton, 2009; Hu et al., 2010; Omidi et al., 2011). Hu and Denton (2009), and Hu et al. (2010) found that EMIC waves firstly grow in the equator region, and they have small WNA and near left-handed polarization. These waves propagate along the magnetic field line toward higher latitudes, and become linearly polarized with a larger WNA. By analyzing the transverse components of EMIC waves in a dipole magnetic field, Omidi et al. (2011) found that one transverse component vanished and the waves become compressible when the waves propagate toward higher latitudes, and they conclude that the polarization of the waves change from the left-handed polarization to the linear polarization. Denton (2018) compared the simulated dispersion relation with the linear theory, and found that the waves turn linearly polarized when approaching the crossover frequency. However, the WNA of EMIC waves has not been quantitatively calculated in these works, and then an accurate diagnosis of ellipticity compared with theoretical ellipticity is impossible. In this work, we try to accurately quantify the characteristics of EMIC waves, and compare the ellipticity with theory, thus determining the effect that is responsible for the polarization change.

In this paper, we employ a 2D general curvilinear particle-in-cell (gcPIC)-hybrid simulation code to study the propagation of EMIC waves excited by the proton temperature anisotropy in a dipole magnetic field. We tract down the behavior of a single wave packet along its path toward higher latitudes. The peak frequency of the packet (the wave mode with the maximum amplitude) is found to decrease as propagating to higher latitudes. We propose a novel method called Wave Front Shape Identification (WFSI) for WNA diagnosis in 2D simulation, which aids us in accurate measurement the WNA of the wave packet. With the accurate diagnosis of wave frequency, WNA and background plasma conditions, the ellipticity can then be calculated using the linear theory, which shows excellent agreement with the diagnosed ellipticity, thus demonstrating that linearly polarized EMIC waves can be caused when they propagate toward high latitudes and the wave normal angle (WNA) become sufficiently large.

2. Simulation Model

In this paper, we employ gcPIC code to investigate the propagation of EMIC waves in a dipole magnetic field. gcPIC is a software package based on kinetic simulations, which is developed in the general curvilinear coordinate system (Lu et al., 2019). gcPIC-hybrid is the hybrid simulation code in gcPIC package. In the hybrid simulation model, electrons are treated as a massless fluid, while ions are considered as particles.

The 2-D gcPIC-hybrid code uses a dipole magnetic field as the background magnetic field $\boldsymbol{B}_0$. To accommodate this geometry, the code uses a modified dipole coordinates system, which is based on the standard 2-D dipole coordinate

$$\mu = -\frac{\sin \lambda}{r^2}, \tag{1}$$

$$\chi = \frac{\cos^2 \lambda}{r}, \tag{2}$$

where r and λ are the distance to the Earth's center and latitude, respectively. The modified 2-D dipole coordinates (p, q) are defined as

$$p = \frac{1}{\chi} = L, \tag{3}$$

$$aq^3 + bq = \mu, \tag{4}$$

in which L is the equatorial distance to the center of the Earth of the field line which passes through a given location. We set the constants $a = 4/L_0^2$, $b = 1/L_0^2$, where L_0 is the L value at the center of the simulation region. Here, (p, q) forms a set of orthogonal coordinates. A constant p describes a single magnetic field line, and a

higher q represents the higher latitude. Such a modified dipole coordinate system has already been successfully used in our gcPIC simulation code to study the excitation of chorus waves in the inner magnetosphere.

In this simulation, we have three particle species: cold electrons, cold isotropic protons and hot anisotropic protons. At the center of simulation region, the total electron density n_{e0}, parallel temperature of hot protons $T_{p0\parallel}$, and magnetic field B_0 satisfy $\omega_{pe0}/\Omega_{e0} = 2.225$ and $V_{A0}/V_{pr0\parallel} = 3.21$, where $\omega_{pe0} = \sqrt{n_{e0}e^2/m_e\varepsilon_0}$ is the plasma frequency, $\Omega_{e0} = eB_0/m_e$ is the electron gyrofrequency, $V_{A0} = B_0/\sqrt{\mu_0 m_p n_{e0}}$ is the Alfven speed, and $V_{pr0\parallel} = \sqrt{T_{p0\parallel}/m_p}$ is the parallel thermal velocity of hot protons (all these values are calculated at the center of simulation region), $m_e, m_p, e,$ and μ_0 are electron and proton mass, elementary charge and dielectric constant and permeability in vacuum. The simulation region is defined by $622.5\rho_{i0} < p < 933.7\rho_{i0}, -1.5 < q < 1.5$, where $\rho_{i0} = V_{pr0\parallel}/\Omega_{p0}$ is the proton gyroradius. Setting the corresponding realistic value of $n_{e0} = 3cm^{-3}, T_{p0\parallel} = 10keV$ and $B_0 = 249.6nT$, ρ_{i0} corresponds to a realistic value of $40.94km$. This leads to an L shell of about $4R_E < L < 6R_E$, and the latitude spread is about $-40° \sim 40°$, as shown in Figure 1. We use a grid of $n_p \times n_q = 256 \times 1024$, and each grid has 500 ion superparticles. The boundary condition for fields is the conductive condition, while the condition for particles is the reflection condition. In addition, there is another "damping" boundary condition for particles which is discussed in details in (Hu & Denton, 2009). The time step is set to be $\Delta t = 0.01\Omega_{p0}^{-1}$.

The cold protons are spatially uniformly loaded. The temperature of cold electrons and protons are set to be $0.0001T_{p0\parallel}$, and on the equator the hot protons have an anisotropy $A_{eq} = \frac{T_{p0\perp}}{T_{p0\parallel}} - 1 = 9$, where $T_{p0\perp}$ is the perpendicular temperature of hot protons on the equator. On the equator hot proton makes up 10% of the total protons. Away from equator the temperature and density of hot protons are set up according to the parallel force balance using the same method described in detail (Lu et al., 2019). The cold electron density is calculated by assuming the plasma to be neutral. The resulted density and temperature anisotropy profile of hot protons are shown in Figure 1.

3. Simulation Results and Analysis

3.1. Wave Fields and Wave Packets

Figure 2 shows the evolution of azimuthal component of fluctuated magnetic field. EMIC waves grow from random noises at the equatorial source region (LAT within 10°), and form clear wave fronts starting at about $t = 100\Omega_{p0}^{-1}$. The waves then propagate toward higher latitudes, meanwhile becoming oblique.

From the evolution of wave fields, we can see that the waves do not form a continuous, wide-spread wave fields, but quickly split into several discrete wave packets after being generated at the equatorial region. These individual wave packets are spatially separated from each other and propagate independently. To see these wave packets more clearly, we calculate the Poynting flux of the wave fields as shown in Figure 3. Red color means propagating northward, and blue color means propagating southward. We then can recognize an isolated red or blue region as a wave packet. In fact, we can even trace the trajectory of one wave packet, which is denoted by "WP" in the figure. The black solid line in Figure 3 is the trajectory of the largest wave packet. We can then analyze the wave properties of this wave packet along its path in detail.

Figure 4a shows the time evolution of the magnetic field B_ϕ at the black dot marked by the notation "A" in Figure 3b ($x = 5.205R_E, y = 0.457R_E$). Because the wave packet "WP" reaches this location at $\Omega_{p0}t \approx 110$, we can find obvious waveform from that time. The wave packet passes through the location "A" at $\Omega_{p0}t \approx 180$. Therefore, we can know the wave frequency after Fourier transforming the magnetic field B_ϕ from $\Omega_{p0}t \approx 110$ to 180. The wave spectrum is shown in Figure 4b, and the peak frequency (the wave mode with the maximum amplitude) is $\omega \approx 0.546\Omega_{p0}$.

Using this method, we can analyze the wave packet frequency along its path. The result is shown in Figure 5. We see that the frequency of wave packet continuously decreases as wave packet propagating to higher latitudes. This is because the wave packet is not monochromic but consists of a band of frequency components (as seen from the spectrum in Figure 4b), and different wave modes have different growth/damping rate at different locations along or near the trajectory of the wave packet. In general, a higher anisotropy tends to have a larger growth rate at higher frequency, and from the simulation we can know that the hot proton anisotropy decreases with latitude (see Figure 1b). Therefore, as the wave packet propagates away from the equator where the anisotropy is the largest, the initial high frequency components get damped or get overcome by newly grown lower frequency components
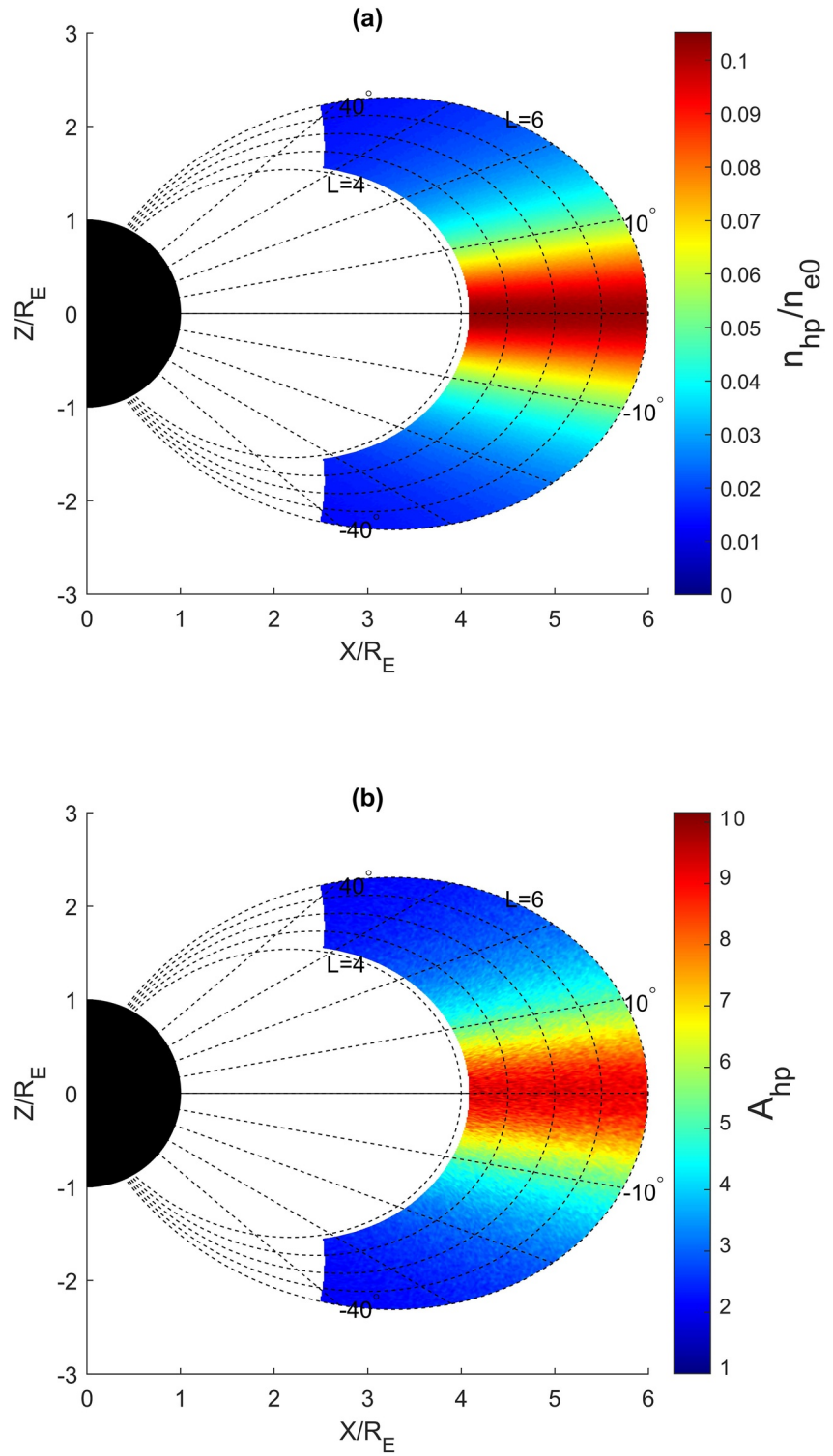
Figure 1. Initial setup of hot proton species. (a) spatial distribution of hot proton density n_{ph}; (b) spatial distribution of hot proton anisotropy $A_{ph} = \frac{T_{ph\perp}}{T_{ph\parallel}} - 1$.
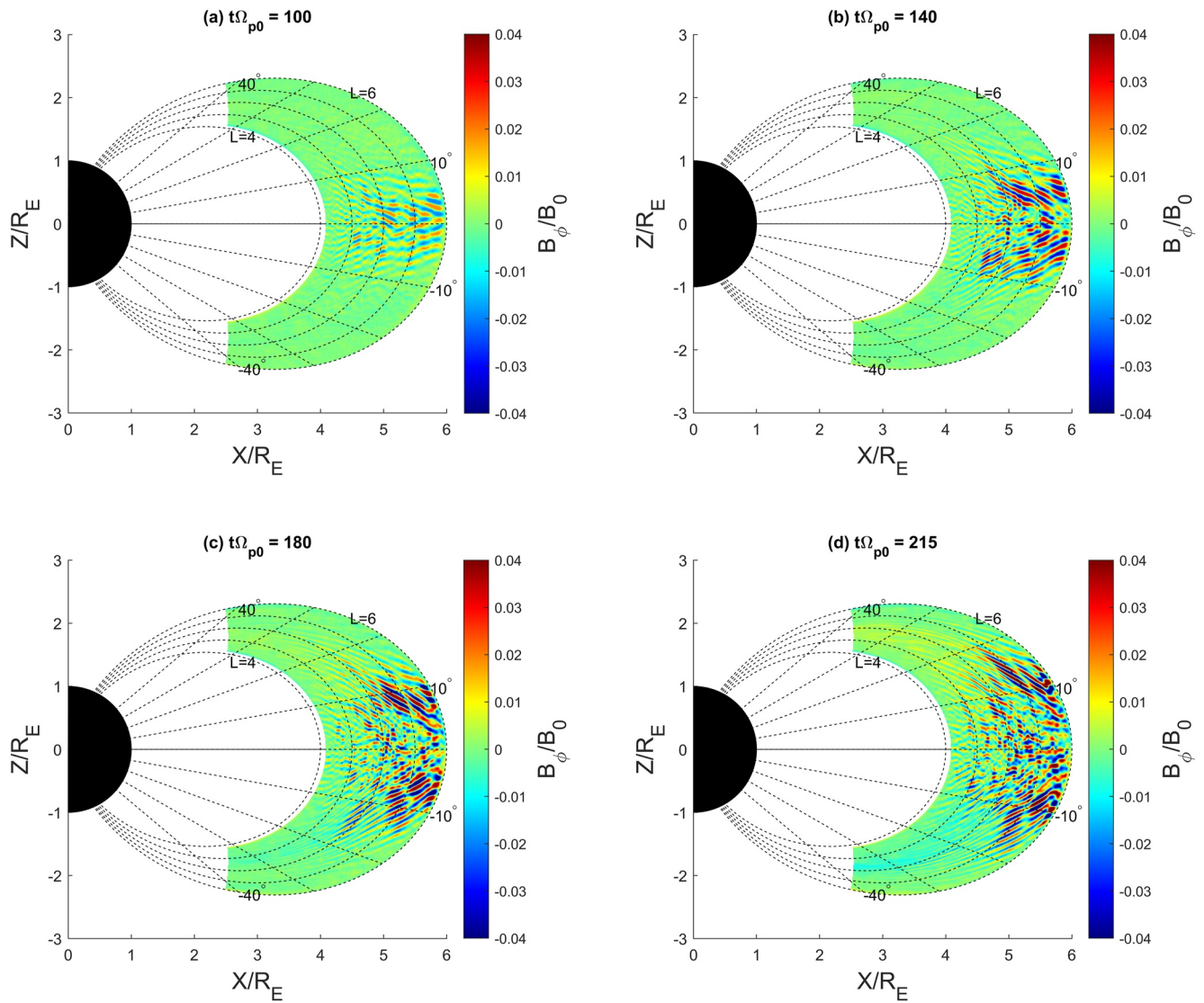
Figure 2. Temporal evolution of the azimuthal component B_ϕ of the EMIC waves. The inner field line corresponds to $L = 4$, while the outer field line corresponds to $L = 6$. The interval between field lines $\Delta L = 0.5$. The latitude between radial dashed lines is 10°.

propagating to the packet's location. The overall effect is then the peak of wave spectrum continuously drifts toward lower frequency. It is not simply a propagation effect, but rather a propagation-induced generation effect. The phenomenon of wave frequency decreasing due to decreasing anisotropy is also reported in previous 1D simulation of EMIC waves (Guo, 2016) and chorus waves (Chen et al., 2017, 2021). The difference is that in these 1D simulations the anisotropy decreases temporally due to free energy consumption, but in our work the anisotropy decreases mainly spatially due to wave packet propagation.

3.2. Wave Normal Angle (WNA)

We propose a novel method, called Wave Front Shape Identification (WFSI), to perform WNA calculation, which makes full use of the following two advantages in the 2D simulation: (a) a 2D simulation guarantees that the wave vector has no azimuthal component, that is, the wave vector must lie within the simulation plane; (b) unlike in situ observation, we have the knowledge of global distribution of wave fields in the simulation. The idea of this method is that when waves are nearly plane waves, the wave fronts are straight lines and the wave normal is perpendicular to the wave fronts. We then fit a straight line from the spatial distribution of wave amplitude to
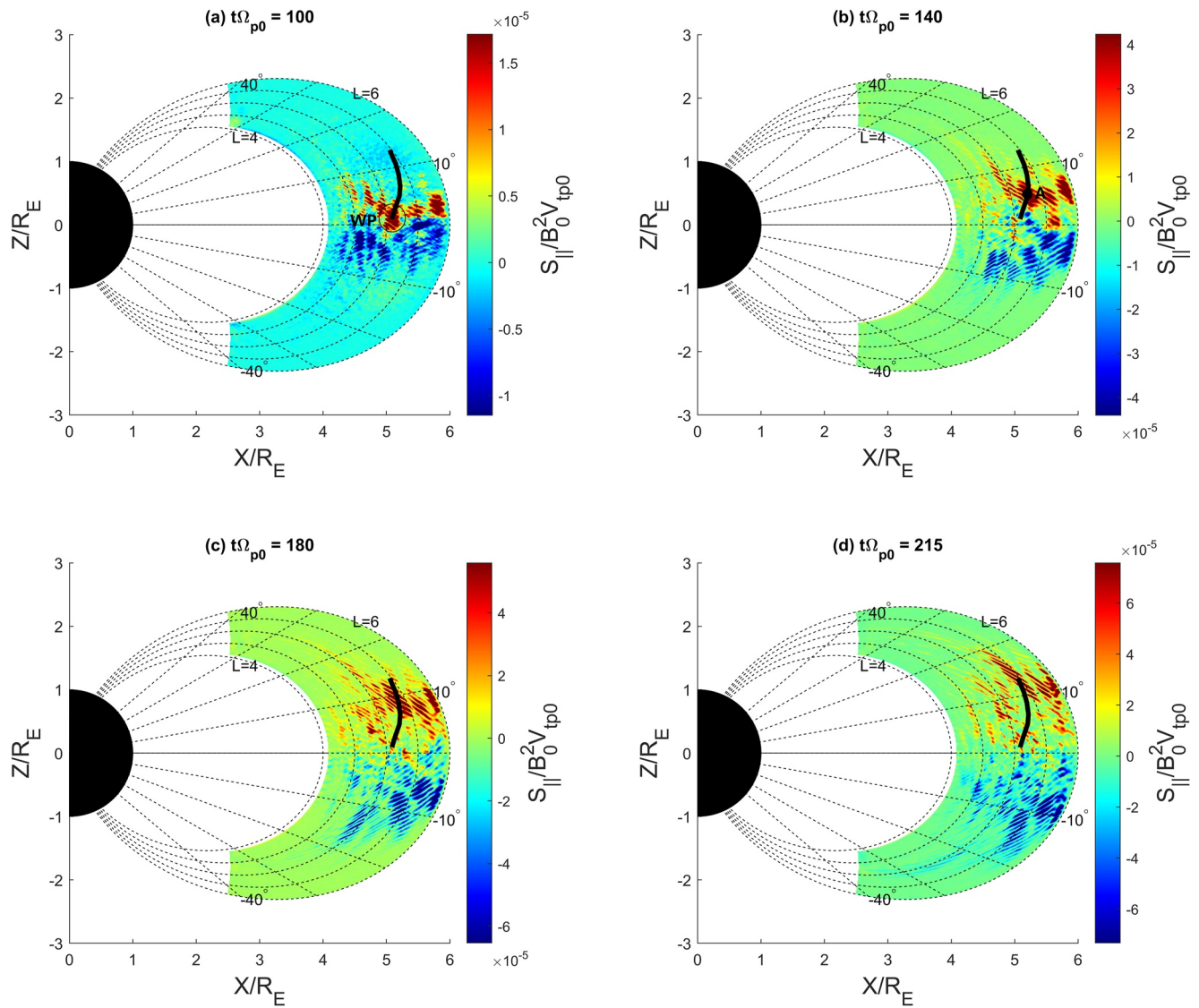
Figure 3. Temporal evolution of Poynting flux and trajectory of a wave packet. The dashed lines and texts are the same with Figure 2. The black solid line marks the trajectory of the wave packet.

represent the shape of a wave front, and find the wave vector parallel to the normal of the fitted line. This method is explained in details as follows.

Figure 6a shows the wave fields of the wave packet at $t\Omega_{p0} = 140$. Firstly, we extract all grid points that make up a single wave front, for example, the second wave front from top to bottom in Figure 6a, which has a positive amplitude. In practical term, this is done by manually selecting a zonal region which completely contains the given wave front, for example, the region between the two gray lines in Figure 6a, and we can find all grid points within that region that have positive amplitudes. Secondly, to reduce the impact of the irregular shape of the wave front boundary, we identify the grid point that has the maximum amplitude $B_{\phi,\max}$, and discard the grid points whose amplitude is lower than $B_{\phi,\max}/2$. The remaining grid points are marked by black dots in Figure 6a and colored dots in Figure 6b. Finally, we use the coordinates of these grid points (x_j, z_j) to fit a straight line $z = ax + b$ using the least square method, which should then represent the shape of the wave front. To better reflect the shape of wave front, we use the ratio $B_{\phi,j}/B_{\phi,\max}$ as a weight when conducting the fitting, where $B_{\phi,j}$ is the wave amplitude at j th grid point. The weight of each grid points is marked by the color of dots in Figure 6b. In that way, the fitted line would more likely to pass through the region with a larger amplitude, thus better represent the
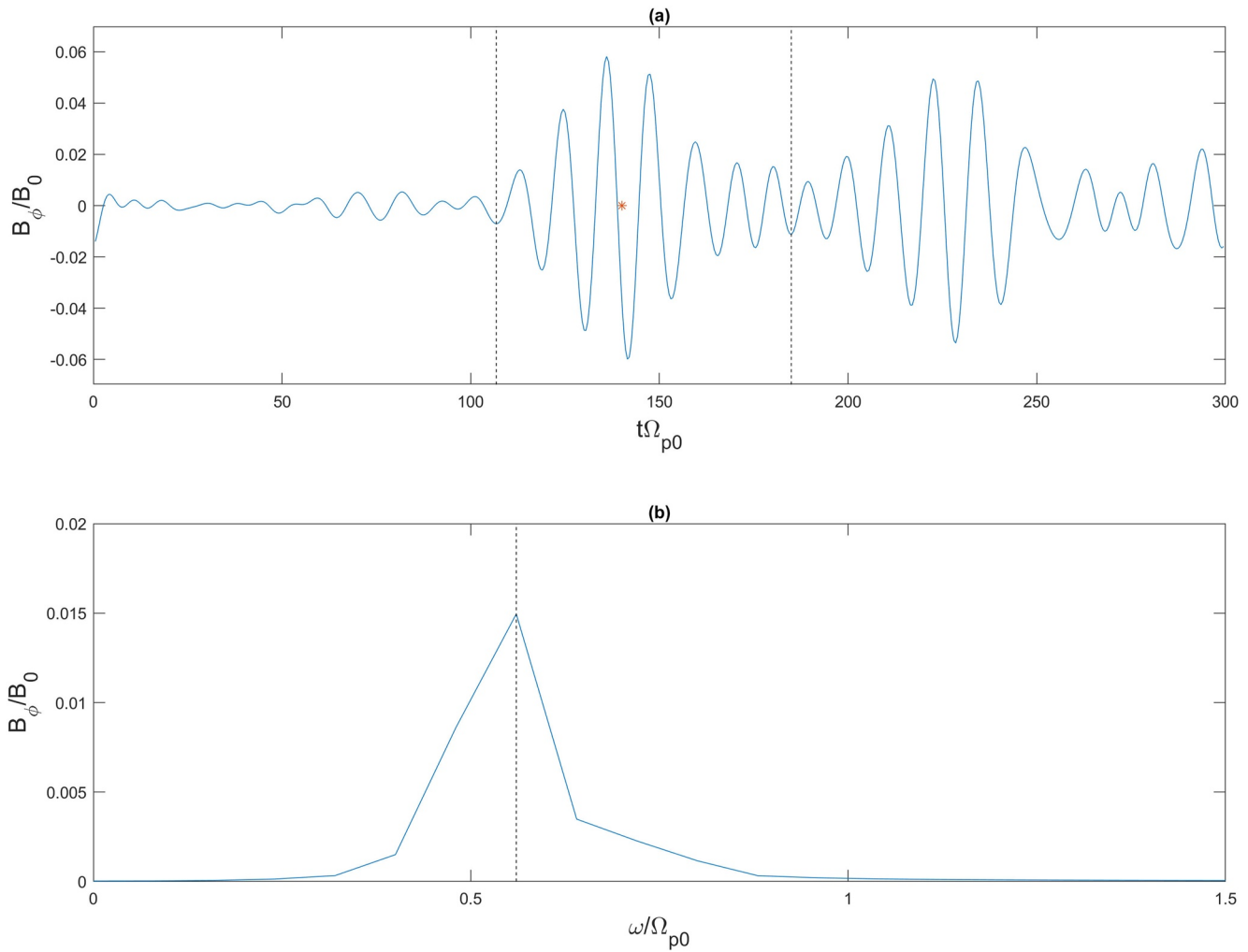
Figure 4. (a) Temporal evolution of B_ϕ at location $x = 5.205 R_E$, $y = 0.457 R_E$. The red star marks the time $t = 140\Omega_{p0}^{-1}$ at which the wave packet pass through the location, and the two black dashed lines marks the time interval during which the wave packet propagates through this point; (b) wave spectrum of the wave packet in (a). The spectrum peaks at $\omega = 0.5567\Omega_{p0}$.

shape of wave front. The fitted line is shown by the black solid line in both Figures 6a and 6b, which indeed well represents the shape and orientation of the wave front.

In 2D simulation the wave vector must lie within the simulation plane, the wave vector can be determined from the slope of the fitted line that represents the shape of wave front:

$$\hat{k} = \hat{x} \frac{a}{\sqrt{1 + a^2}} - \hat{z} \frac{1}{\sqrt{1 + a^2}}, \tag{5}$$

where a is the slope of the fitted line. To further reduce the error, we can fit multiple wave fronts (for example, in Figure 6 two wave fronts are fitted), and insert the average slope $\bar{a} = \frac{1}{N} \sum_{i=1}^{N} a_i$ into Equation 1 to calculate the wave vector. Combined with the direction of local magnetic field we can then calculate the WNA of wave packet at the given location. Applying this WFSI method we obtain the WNA evolution of the wave, as shown in Figure 7. We see that the WNA increases as the wave packet propagates to higher latitude.
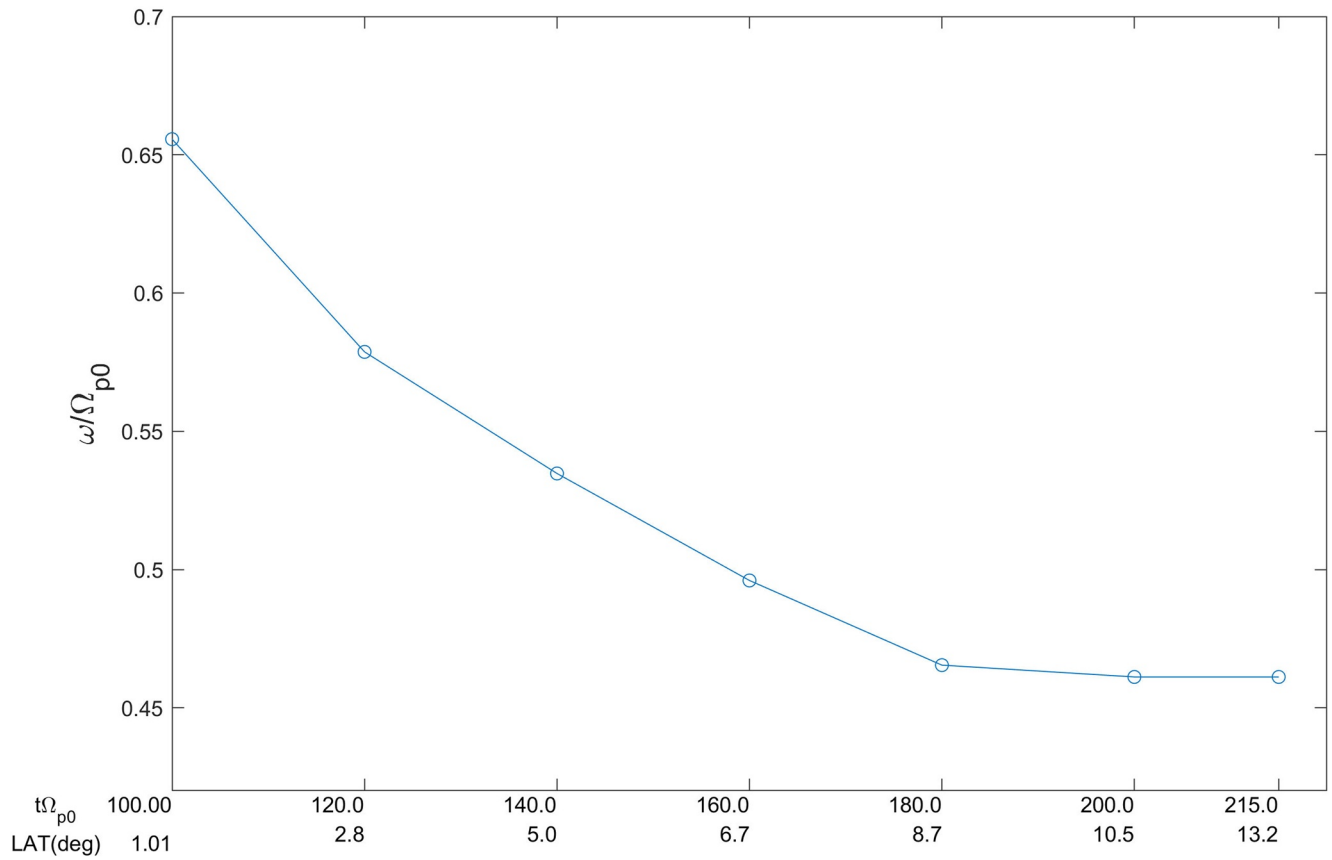
Figure 5. Evolution of frequency of the wave packet. The first line of *x* axis label is the time $t\Omega_{p0}$, and the second line of *x* axis label is the latitude (LAT) of the wave packet.
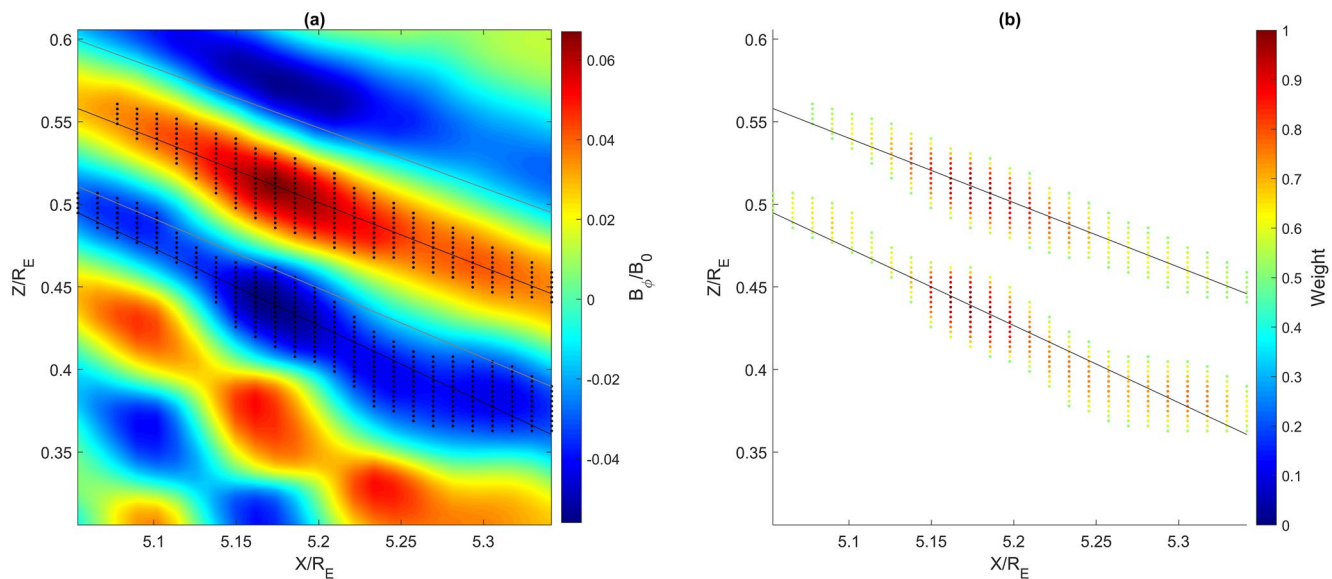

Figure 6. Illustration of the linear fitting method for WNA diagnosis. (a) The pattern of wave fields. The two gray lines marks a zonal region which contain one complete wave front, the black dots are the grid points that make up a wave fronts, and the black solid lines are the fitted lines that represent the shape of the wave fronts; (b) The selected grid points. The color of point represents the weight of this point when conducting the fitting. The black solid lines are the fitted lines that represent the shape of the wave fronts.
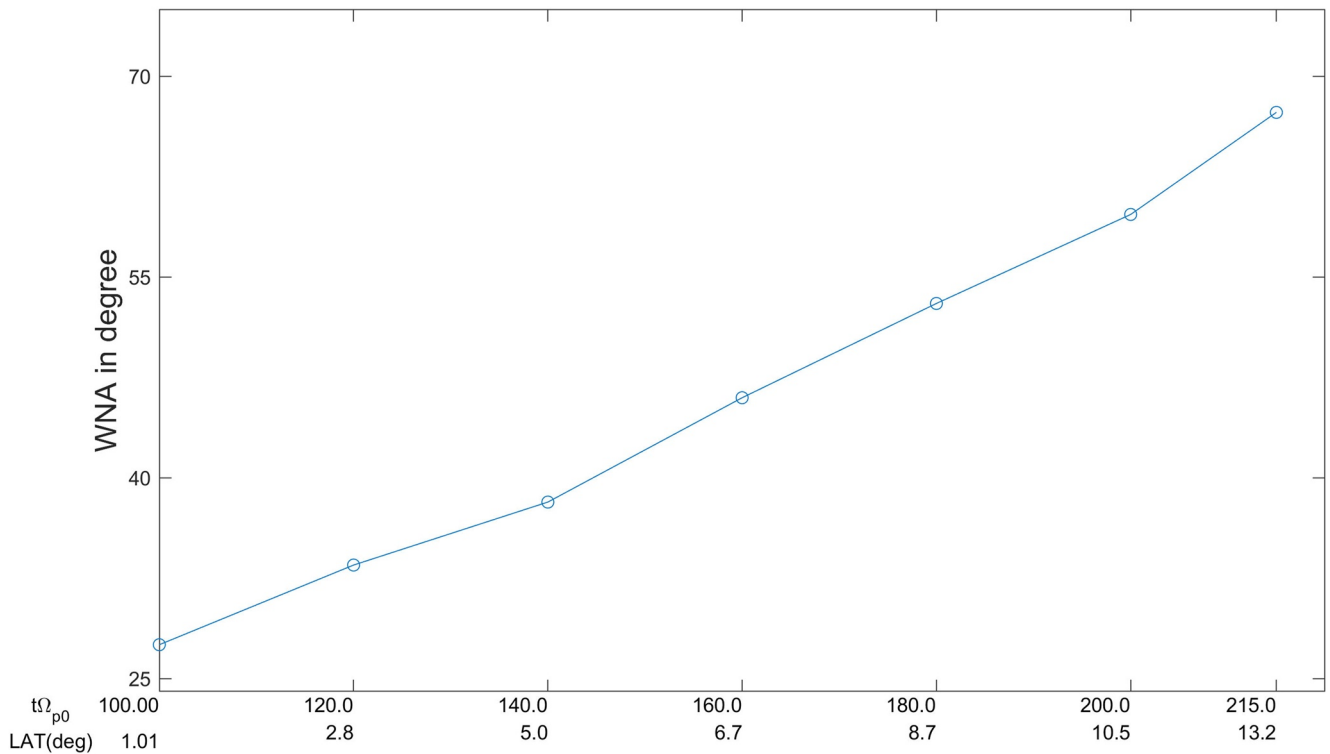
Figure 7. The evolution of wave normal angle of the wave packet with the same x axis labels as Figure 5.

3.3. Polarization

After we know the WNA of the wave packet based on the WFSI method, we can plot the hodogram of its perpendicular components $\delta B_\perp$ in the wave frame, as shown in Figure 8a. The ellipticity ϵ is defined as the ratio of the major and minor axes:

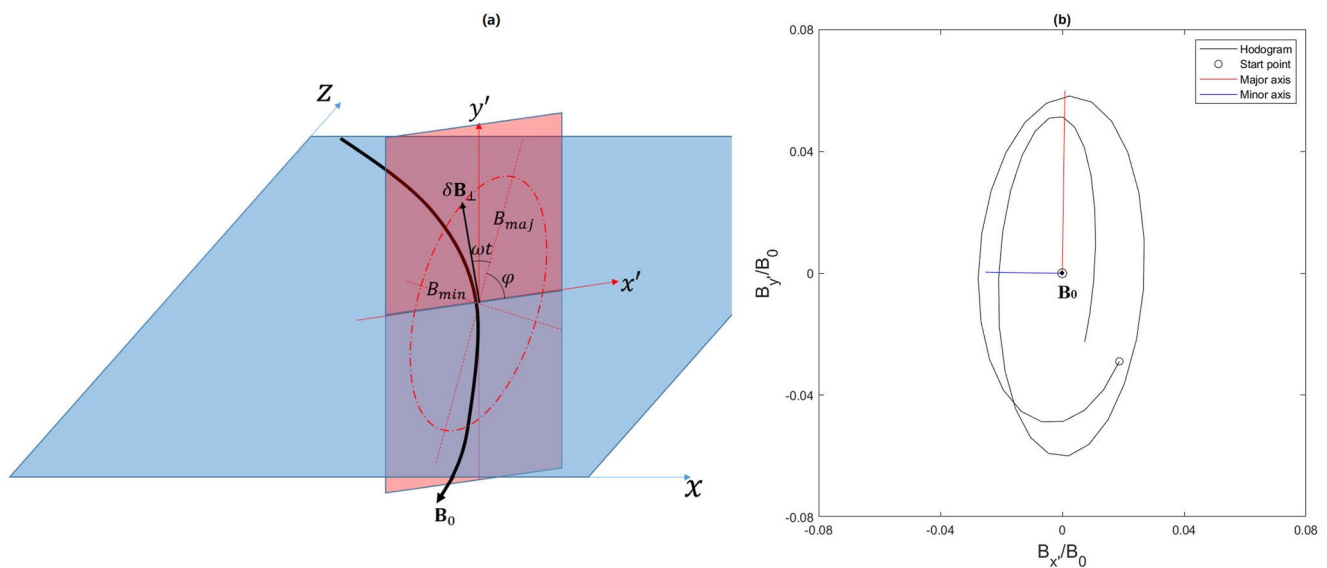**Figure 8.** (a) illustration of the elliptically polarized $\delta B_\perp$ components. The blue plane is the simulation plane, and the red plane is the plane perpendicular to local background magnetic field B_0. y' axis is perpendicular to simulation plane, and x' axis is perpendicular to B_0 while lies in the simulation plane; (b) hodogram of $\delta B_\perp$ at $x = 5.205 R_E$, $y = 0.457 R_E$ during $128.5\Omega_p^{-1} < t < 151.5\Omega_p^{-1}$. The black circle marks the start point of the hodogram, and the blue and red lines mark the direction of minor and major axes, respectively. The direction of background magnetic field is out of page.

$$\epsilon = \frac{B_{\text{min}}}{B_{\text{maj}}}, \tag{6}$$

where B_{maj} and B_{min} are the major and minor axes shown in Figure 8a. Assuming that $\delta \boldsymbol{B}_{\perp}$ has a frequency ω and an initial phase φ, then $\delta \boldsymbol{B}_{\perp}$ can be written as

$$\delta \boldsymbol{B}_{\perp} = \hat{\boldsymbol{x}}' B_{\text{maj}} \cos(\omega t + \varphi) + \hat{\boldsymbol{y}}' B_{\text{min}} \sin(\omega t + \varphi), \tag{7}$$

where the direction $\hat{\boldsymbol{x}}'$ and $\hat{\boldsymbol{y}}'$ are indicated in Figure 8a. We define a matrix $\boldsymbol{M}$ as

$$\boldsymbol{M} = \int_0^T \delta \boldsymbol{B}_{\perp} \delta \boldsymbol{B}_{\perp} dt = \int_0^{\frac{2\pi}{\omega}} \begin{pmatrix} \delta B_{x'} \delta B_{x'} & \delta B_{x'} \delta B_{y'} \\ & \\ \delta B_{x'} \delta B_{y'} & \delta B_{y'} \delta B_{y'} \end{pmatrix} dt, \tag{8}$$

where $T = \frac{2\pi}{\omega}$ is the period of waves. Using Equation 3, we have

$$\boldsymbol{M} = \frac{\pi}{\omega} \begin{pmatrix} B_{\text{maj}}^2 \cos^2 \varphi + B_{\text{min}}^2 \sin^2 \varphi & (B_{\text{maj}}^2 - B_{\text{min}}^2) \cos \varphi \sin \varphi \\ (B_{\text{maj}}^2 - B_{\text{min}}^2) \cos \varphi \sin \varphi & B_{\text{maj}}^2 \cos^2 \varphi + B_{\text{min}}^2 \sin^2 \varphi \end{pmatrix}, \tag{9}$$

which can be diagonalized to find two eigenvalues

$$\lambda_1 = \frac{\pi B_{\text{maj}}^2}{\omega}, \quad \lambda_2 = \frac{\pi B_{\text{min}}^2}{\omega}, \quad \lambda_1 \geq \lambda_2, \tag{10}$$

with their eigenvectors being the major and minor axes, respectively. Therefore, we can obtain the ellipticity by

$$\epsilon = \sqrt{\frac{\lambda_2}{\lambda_1}}. \tag{11}$$

We use the algorithm described above to calculate the ellipticity of wave packet at a given location, for example, at $(x = 5.205 R_E, y = 0.457 R_E)$, the location of wave packet at $t_0 = 140\Omega_{p0}^{-1}$. We extract the waveform of the $\delta \boldsymbol{B}_{\perp}$ at this location during the interval $t_0 - \frac{2\pi}{\omega} < t < t_0 + \frac{2\pi}{\omega}$, where $\omega = 0.546\Omega_{p0}$ is the frequency obtained in Section 3.2. The hodogram of $\delta \boldsymbol{B}_{\perp}$ during this period is shown in Figure 8b. The black circle marks the starting point of the hodogram. Along the direction of background magnetic field (marked in Figure 8b), we can see that the rotation direction of $\delta \boldsymbol{B}_{\perp}$ is left-handed using the right-hand rule. The overall shape of this hodogram is indeed an ellipse. Applying the method described above we find the ellipticity is about -0.43, and the major and minor axes are marked as the blue and red lines, respectively.

Using the methods described above we find the evolution of ellipticity along the path of the wave packet as shown by the blue line in Figure 9. The ellipticity increases from about -0.75 to nearly 0, which indicates the polarization of wave packet turns from a left-handed polarization to a linear polarization. We also notice that the evolution of ellipticity and WNA is correlated to each other because they show very similar tendency, which indicates the polarization change here is due to waves turning oblique.

To verify this hypothesis, we compare the ellipticity calculated based on wave data obtained in the simulation with the ellipticity calculated based on the linear theory (theoretical ellipticity). We use the linear dispersion solver PDRK (Xie & Xiao, 2016) to calculate the theoretical ellipticity. Determining the theoretical ellipticity requires the knowledge of: (a) the shape of dispersion surface; (b) the location of wave packet on the dispersion surface. Calculating the dispersion relation requires the local plasma condition (density and temperature of each species and local magnetic field), which is also available from the simulation. We specify the location of wave packet on the dispersion surface by specifying wave frequency and WNA, which are calculated in Sections 3.1 and 3.2, respectively.

The simulated and theoretical ellipticity is shown in Figure 9. We see that the simulated ellipticities coincide with the theoretical ones very well. This reveals that the polarization change of EMIC wave packet is solely due to the propagation effect that EMIC waves turn oblique when propagating toward high latitudes.
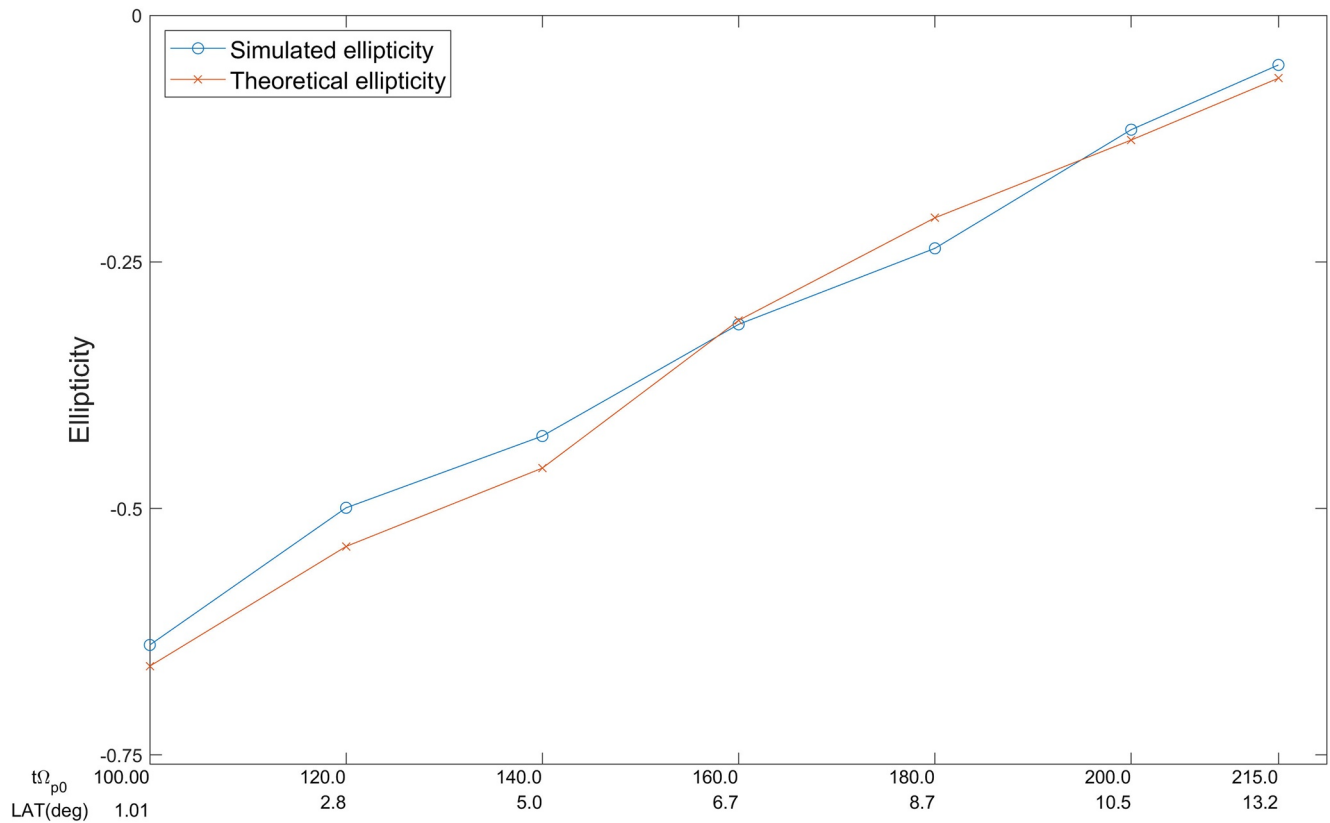
Figure 9. Comparison of simulated and theoretical ellipticity. The blue line is the simulated ellipticity, and the red line is the theoretical ellipticity. The x axis labels are the same as Figure 5.

4. Discussion

One main reason why we do not use the conventional MVA method (e.g., Sonnerup & Cahill, 1967; Means, 1972; Santolik et al., 2003) to find the WNA is that the evolution of waves in our simulation is much too quick. Either by working on time domain like Sonnerup and Cahill (1967) or working on frequency domain like Means (1972) or Santolik et al. (2003), correctly analyzing the direction of wave vector requires a sufficiently long and stable duration of waves. This is even more fatal if one chooses to work on frequency domain because a reliable FFT with sufficient resolution puts strict limits on the length of time window (e.g., to achieve a resolution of 1/10 of the wave frequency ω, a time window at least $2\pi/0.1\omega = 10T$, T is the period of wave). In comparison to the example in Figure 4a, the wave amplitude changes dramatically within just three periods. Therefore, MVA method leads to obviously incorrect wave vector direction in our simulation data analysis: it gives wave vectors that have comparable x' and y' components (x', y' directions are illustrated in Figure 8a), where the y' component should not exist at all due to the 2D nature of the simulation.

In contrast, our novel WFSI method ensures a very accurate WNA as long as the wave packet can be well approximated by plane waves (so that the wave front would be a straight line and the wave vector would be perpendicular to the wave front). The WFSI method does not require any operation on the time domain, so it is applicable even when waves evolve too fast. The WFSI method is especially suitable for 2D simulations where the spatial distribution of electromagnetic fields is available, and its philosophy can be easily extended to 3D simulations. The WFSI method also have potential application in laboratory plasma experiments because in laboratory experiments it is also possible to obtain the spatial distribution of wave fields. Such application is very appealing because waves in laboratory experiments usually encounter the same situation as we do: waves evolve too fast, and wave duration is short, therefore the MVA method should also leads to great errors. After we know the WNAs of the excited EMIC waves, the ellipticity is easy to be determined by plotting the hodogram of the perpendicular components $\delta\boldsymbol{B}_\perp$ in the wave frame (e.g., Anderson et al., 1996).

Previous works on EMIC wave simulation in a dipole field have reported the phenomenon that EMIC waves turn oblique and turn to linear polarization as they propagate toward higher latitudes. However, although many of them suggest that turning oblique could be the cause of turning to a linear polarization, none of them check that the values of WNA matches theoretically with the values of ellipticity, and none of them rule out other potential factors that could cause the polarization change. In one word, none of them gives strict proof for the causality between EMIC waves' turning oblique and turning to linear polarization, but merely give a suggestion.

In our work, we exclude the crossover effect because we introduce no heavier ion species. We use a bi-Maxwellian distribution for EMIC wave generation, and the initial plasma $\beta \approx 0.3$ is also small, therefore we also exclude the generation effects, and we indeed observe that the EMIC waves generated near the equator are left-handed polarized. Moreover, the single wave packet we trace does not cross any other wave packets, so there is no superposition effect. Finally, we qualitatively compare the simulated ellipticities with the theoretical ellipticities corresponding to the simulated WNA, and find good agreement between them. Therefore, we conclude that the propagation effect of waves turning oblique agree with the linear polarization of the EMIC waves qualitatively, and this is the only effect that plays a role in the polarization change in our electron-proton plasma model.

5. Conclusions

Using a 2D hybrid code we simulate the propagation of an EMIC wave packet. Multiple discrete wave packets are generated from the equatorial region, which are excited by the proton temperature anisotropy. We trace one of the wave packets and analyze its spectrum, WNA and polarization evolution along its trajectory. We find that in contrast with the general belief that the frequency of waves is a constant, the peak frequency of the wave packet decreases when the waves propagate toward higher latitudes. The decrease of the peak frequency of the packet is generated because the different wave modes has different growth and damping behavior, and when the packet propagates to high latitudes the amplitude of the lower frequency modes exceeds that of the higher frequency modes. We also reproduce the phenomena that waves become more and more oblique as waves propagate to high latitudes, with that the polarization of EMIC waves change from left-handed polarized to linearly polarized. By comparing the ellipticity calculated directly from wave field data (simulated ellipticity) with the ellipticity calculated from linear theory (theoretical ellipticity), we confirm that in a plasma whose only ion species is proton, the polarization change is solely due to the propagation effect that waves become oblique while propagating to high latitude.

Data Availability Statement

Our data can be accessed from https://dx.doi.org/10.12176/01.99.00701. The source code we use to realize the WFSI method can be accessed from https://dx.doi.org/10.12176/01.99.01544.

References

Allen, R. C., Zhang, J. C., Kistler, L. M., Spence, H. E., Lin, R. L., Klecker, B., et al. (2015). A statistical study of EMIC waves observed by Cluster: 1. Wave properties. *Journal of Geophysical Research: Space Physics*, *120*(7), 5574–5592. https://doi.org/10.1002/2015JA021333

Anderson, B. J., Denton, R. E., & Fuselier, S. A. (1996). On determining polarization characteristics of ion cyclotron wave magnetic field fluctuations. *Journal of Geophysical Research*, *101*(13). https://doi.org/10.1029/96ja00633

Anderson, B. J., Erlandson, R. E., & Zanetti, L. J. (1992). A statistical study of Pc 1–2 magnetic pulsations in the equatorial magnetosphere: 2. Wave properties. *Journal of Geophysical Research*, *97*(A3), 3089–3101. https://doi.org/10.1029/91JA02697

Anderson, B. J., Takahashi, K., Erlandson, R. E., & Zanetti, L. J. (1990). Pc1 pulsations observed by AMPTE/CCE in the Earth's outer magnetosphere. *Geophysical Research Letters*, *17*(11), 1853–1856. https://doi.org/10.1029/GL017i011p01853

André, M. (1985). Dispersion surfaces. *Journal of Plasma Physics*, *331*, 1–19.

Chen, H., Gao, X., Lu, Q., Ke, Y., & Wang, S. (2017). Lower band cascade of whistler waves excited by anisotropic hot electrons: One-dimensional PIC simulations. *Journal of Geophysical Research: Space Physics*, *122*(10), 10448–10457. https://doi.org/10.1002/2017JA024513

Chen, H., Gao, X., Lu, Q., Sauer, K., Chen, R., Yao, J., et al. (2021). Gap formation around 0.5 Ωe of whistler-mode waves excited by electron temperature anisotropy. *Journal of Geophysical Research: Space Physics*, *126*(2). https://doi.org/10.1029/2020JA028631

Chen, H., Gao, X., Lu, Q., Tsurutani, B. T., & Wang, S. (2020). Statistical evidence for EMIC wave excitation driven by substorm injection and enhanced solar wind pressure in the Earth's magnetosphere: Two different EMIC wave sources. *Geophysical Research Letters*, *47*(21). https://doi.org/10.1029/2020GL090275

Chen, H., Gao, X., Lu, Q., & Wang, S. (2019). Analyzing EMIC waves in the inner magnetosphere using long-term Van Allen Probes observations. *Journal of Geophysical Research: Space Physics*, *124*, 7402–7412. https://doi.org/10.1029/2019JA026965

Chen, L., Thorne, R. M., Bortnik, J., & Zhang, X. J. (2016). Nonresonant interactions of electromagnetic ion cyclotron waves with relativistic electrons. *Journal of Geophysical Research: Space Physics*, *121*(10), 9913–9925. https://doi.org/10.1002/2016JA022813

Davidson, R. C., & Ogden, J. M. (1975). Electromagnetic ion cyclotron instability driven by ion energy anisotropy in high-beta plasmas. *Physics of Fluids*, *18*, 1045. https://doi.org/10.1063/1.861253

Denton, R. E. (2018). Electromagnetic Ion cyclotron wavefields in a realistic dipole field. *Journal of Geophysical Research: Space Physics*, *123*, 1208–1223. https://doi.org/10.1002/2017JA024886

Denton, R. E., Anderson, B. J., Ho, G., & Hamilton, D. C. (1996). Effects of wave superposition on the polarization of electromagnetic ion cyclotron waves. *Journal of Geophysical Research*, *101.A11*, 24869–24885. https://doi.org/10.1029/96JA02251

Denton, R. E., Hudson, M. K., & Roth, I. (1992). Loss-cone-driven ion cyclotron waves in the magnetosphere. *Journal of Geophysical Research*, *97*(A8), 12093–12103. https://doi.org/10.1029/92JA00954

Denton, R. E., Jordanova, V. K., & Fraser, B. J. (2014). Effect of spatial density variation and O⁺ concentration on the growth and evolution of electromagnetic ion cyclotron waves. *Journal of Geophysical Research*, *119*, 8472–8395. https://doi.org/10.1002/2014ja020384

Denton, R. E., Ofman, L., Shpritts, Y. Y., Bortnik, J., Millan, R. M., Rodger, C. J., et al. (2019). Pitch angle scattering of sub-Mev relativistic electrons by electromagnetic ion cyclotron waves. *Journal of Geophysical Research: Space Physics*, *124*, 5610–5626. https://doi.org/10.1029/2018ja026384

Fraser, B. J. (1985). Observations of ion cyclotron waves near synchronous orbit and on the ground. *Space Plasma Simulations*, 357–374. https://doi.org/10.1007/978-94-009-5454-0_22

Fuselier, S. A., & Anderson, B. J. (1996). Low-energy He+ and H+ distributions and proton cyclotron waves in the afternoon equatorial magnetosphere. *Journal of Geophysical Research*, *101*(A6), 13255–13265. https://doi.org/10.1029/96JA00292

Gary, S. P., & Lee, M. A. (1994). The ion cyclotron anisotropy instability and the inverse correlation between proton anisotropy and proton beta. *Journal of Geophysical Research*, *99*(A6), 11297–11301. https://doi.org/10.1029/94JA00253

Guo, J. (2016). The generation and evolution of multi-band EMIC waves in the magnetosphere: Hybrid simulations. *Advances in Space Research*, *58*, 2460–2468. https://doi.org/10.1016/j.asr.2016.08.012

Hu, Y., & Denton, R. E. (2009). Two-dimensional hybrid code simulation of electromagnetic ion cyclotron waves in a dipole magnetic field. *Journal of Geophysical Research*, *114*, A12217. https://doi.org/10.1029/2009JA014570

Hu, Y., Denton, R. E., & Johnson, J. R. (2010). Two-dimensional hybrid code simulation of electromagnetic ion cyclotron waves of multi-ion plasmas in a dipole magnetic field. *Journal of Geophysical Research*, *115*, A09218. https://doi.org/10.1029/2009JA015158

Xie, H., & Xiao, Y. (2016). PDRK: A general kinetic dispersion relation solver for magnetized plasma. *Plasma Science and Technology*, *18*, 297–107. https://doi.org/10.1088/1009-0630/18/2/01

Li, W., Shprits, Y. Y., & Thorne, R. M. (2007). Dynamic evolution of energetic outer zone electrons due to wave-particle interactions during storms. *Journal of Geophysical Research*, *112*(A10). https://doi.org/10.1029/2007JA012368

Lu, Q. M., Ke, Y., Wang, X., Liu, K., Gao, X., Chen, L., et al. (2019). Two-dimensional gcPIC simulation of rising-tone chorus waves in a dipole magnetic field. *Journal of Geophysical Research: Space Physics*, *124*, 4157–4167. https://doi.org/10.1029/2019JA026586

Ma, Q., Li, W., Yue, C., Thorne, R. M., Bortnik, J., Kletzing, C. A., et al. (2019). Ion heating by electromagnetic ion cyclotron waves and magnetosonic waves in the Earth's inner magnetosphere. *Geophysical Research Letters*, *46*(12), 6258–6267. https://doi.org/10.1029/2019GL083513

Means, J. D. (1972). Use of the three-dimensional covariance matrix in analyzing the polarization properties of plane waves. *Journal of Geophysical Research*, *77*, 5551–5559. https://doi.org/10.1029/JA077i028p05551

Min, K., Lee, J., Keika, K., & Li, W. (2012). Global distribution of EMIC waves derived from THEMIS observations. *Journal of Geophysical Research*, *117*(A5). https://doi.org/10.1029/2012JA017515

Ni, B., Cao, X., Zou, Z., Zhou, C., Gu, X., Bortnik, J., et al. (2015). Resonant scattering of outer zone relativistic electrons by multiband EMIC waves and resultant electron loss time scales. *Journal of Geophysical Research: Space Physics*, *120*(9), 7357–7373. https://doi.org/10.1002/2015JA021466

Omidi, N., Thorne, R., & Bortnik, J. (2011). Hybrid simulations of EMIC waves in a dipolar magnetic field. *Journal of Geophysical Research*, *116*, A9. https://doi.org/10.1029/2011JA016511

Omura, Y., & Zhao, Q. (2012). Nonlinear pitch angle scattering of relativistic electrons by EMIC waves in the inner magnetosphere. *Journal of Geophysical Research*, *117*(A8). https://doi.org/10.1029/2012JA017943

Remya, B., Lee, K. H., Lee, L. C., & Tsurutani, B. T. (2017). Coherency and ellipticity of electromagnetic ion cyclotron waves: Satellite observations and simulations. *Journal of Geophysical Research: Space Physics*, *1223*, 3374–3396. https://doi.org/10.1002/2016JA023588

Santolík, O., Parrot, M., & Lefeuvre, F. (2003). Michel Parrot, and François Lefeuvre. "Singular value decomposition methods for wave propagation analysis. *Radio Science*, *38*, 1. https://doi.org/10.1029/2000RS002523

Smith, R. L., & Brice, N. (1964). Propagation in multicomponent plasmas. *Journal of Geophysical Research*, *6923*, 5029–5040. https://doi.org/10.1029/JZ069i023p05029

Sonnerup, B. U. Ö., & Cahill, L. J., Jr. (1967). Magnetopause structure and attitude from Explorer 12 observations. *Journal of Geophysical Research*, *721*, 171–183. https://doi.org/10.1029/JZ072i001p00171

Thorne, R., & Kennel, C. F. (1971). Relativistic electron precipitation during magnetic storm main phase. *Journal of Geophysical research*, *76*(19), 4446–4453. https://doi.org/10.1029/JA076i019p04446

Thorne, R. M. (2010). Radiation belt dynamics: The importance of wave-particle interactions. *Geophysical Research Letters*, *37*(22). https://doi.org/10.1029/2010GL044990

Thorne, R. M., & Horne, R. B. (1994). Energy transfer between energetic ring current H+ and O+ by electromagnetic ion cyclotron waves. *Journal of Geophysical Research*, *99*(A9), 17275–17282. https://doi.org/10.1029/94JA01007

Young, D. T., Perraut, S., Roux, A., De Villedary, C., Gendrin, R., Korth, A., et al. (1981). Wave-particle interactions near ΩHe+ observed on GEOS 1 and 2 1. Propagation of ion cyclotron waves in He+-rich plasma. *Journal of Geophysical Research*, *86*(A8), 6755–6772. https://doi.org/10.1029/JA086iA08p06755

Yue, C., Jun, C. W., Bortnik, J., An, X., Ma, Q., Reeves, G. D., et al. (2019). The relationship between EMIC wave properties and proton distributions based on Van Allen probes observations. *Geophysical Research Letters*, *46*(8), 4070–4078. https://doi.org/10.1029/2019GL082633

Zhang, X. J., Li, W., Ma, Q., Thorne, R. M., Angelopoulos, V., Bortnik, J., et al. (2016). Direct evidence for EMIC wave scattering of relativistic electrons in space. *Journal of Geophysical Research: Space Physics*, *121*(7), 6620–6631. https://doi.org/10.1002/2016JA022521